

NARVis: Neural Accelerated Rendering for Real-Time Scientific Point Cloud Visualization

Srinidhi Hegde¹ Kaur Kullman² Thomas Grubb³ Leslie Lait³
 Stephen Guimond⁴ Matthias Zwicker¹

¹ University of Maryland, College Park ² University of Maryland, Baltimore County ³ NASA
⁴ Hampton University

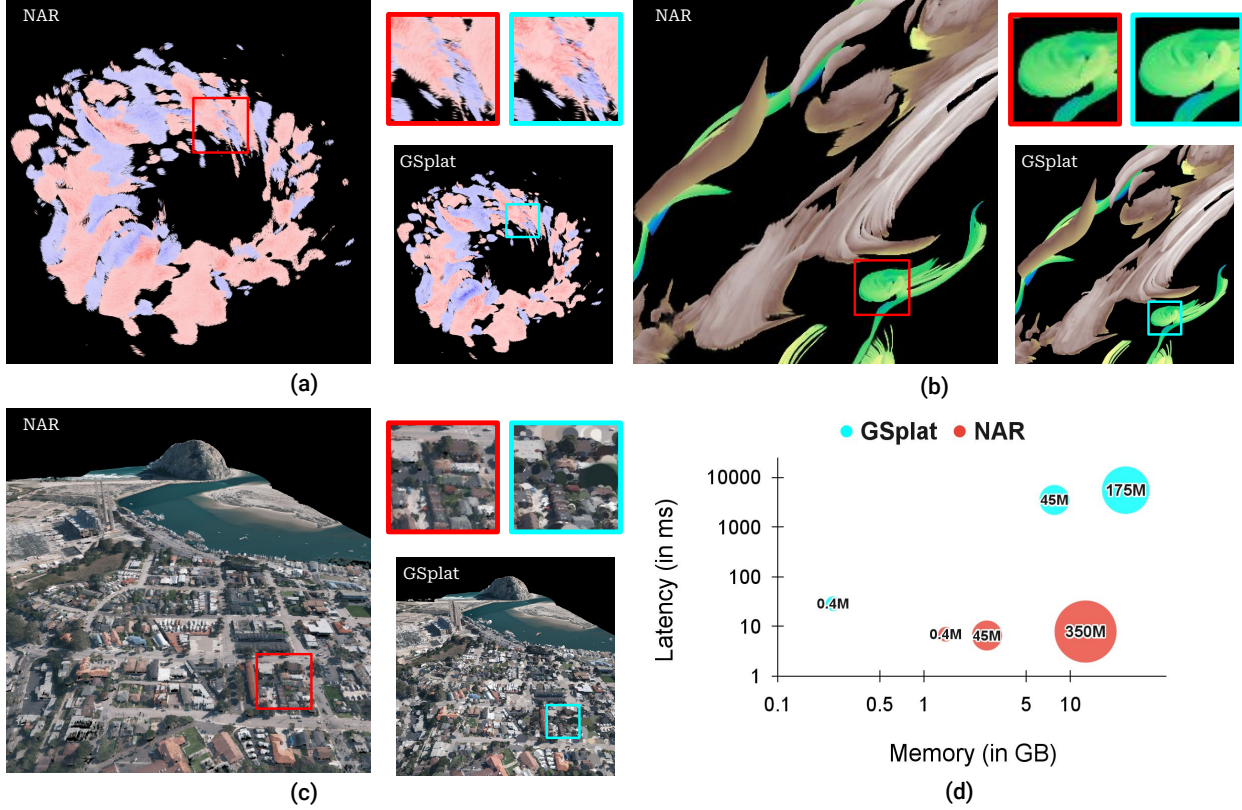


Figure 1. We present Neural Accelerated Renderer (NAR) for high-quality visualization of large scientific point clouds with low motion-to-photon latency. We show that NAR can visualize a variety of scientific use cases, such as visualizing (a) static vector fields (*Hurricane*), (b) particle trajectories (*Storms*), and (c) photometric terrain scans (*Morro Bay*). (d) NAR renders high-quality images comparable to the rendering quality of conventional high-quality renderers (such as the Gaussian Splatting (GSplat) renderer) with significantly lower latency and memory footprints. (Note: the axes are in log-scale and the bubble sizes are proportional to the labeled number of points.)

Abstract

Exploring scientific datasets with billions of samples in real-time visualization presents a challenge - balancing high-fidelity rendering with speed. This work introduces a novel renderer - Neural Accelerated Renderer (NAR), that uses the neural deferred rendering framework to visualize large-scale scientific point cloud data. NAR augments a

real-time point cloud rendering pipeline with high-quality neural post-processing, making the approach ideal for interactive visualization at scale. Specifically, we train a neural network to learn the point cloud geometry from a high-performance multi-stream rasterizer and capture the desired postprocessing effects from a conventional high-quality renderer. We demonstrate the effectiveness of NAR by visualizing complex multidimensional Lagrangian flow

fields and photometric scans of a large terrain and compare the renderings against the state-of-the-art high-quality renderers. Through extensive evaluation, we demonstrate that NAR prioritizes speed and scalability while retaining high visual fidelity. We achieve competitive frame rates of > 126 fps for interactive rendering of $> 350M$ points (i.e., an effective throughput of > 44 billion points per second) using ~ 12 GB of memory on RTX 2080 Ti GPU. Furthermore, we show that NAR is generalizable across different point clouds with similar visualization needs and the desired post-processing effects could be obtained with substantial high quality even at lower resolutions of the original point cloud, further reducing the memory requirements.

1. Introduction

Real-time visualization is integral to the scientific community, offering immediate insights and enhancing decision-making for researchers dealing with complex datasets. When coupled with immersive experiences, such as within extended reality (XR) environments, real-time visualization enriches the user’s understanding of the data, enabling deeper insights [19, 27]. However, visualizing large data volumes from high-throughput simulators [2, 26] poses serious challenges, especially in XR, where low frame rates may cause simulation sickness for its users [17]. Accurate data reproduction, precise rendering, responsive interaction, and coherent visual structures are essential for effective visualizations.

Direct point cloud (PC) rendering methods and tools [1, 37, 39] offer high accuracy within the limits of screen resolution and machine precision. However, these methods often lack the flexibility to incorporate diverse visual constructs, such as glyphs and textures, which is crucial in enhancing the data interpretability [16]. For example, the illustrative visualization paradigm [6, 7] focuses on effective strategies for visualizing complex flow phenomena, like Lagrangian flow fields in fluid simulations (see Figure 1 (a), (b)), and requires rendering the velocity streaks, streamlines, transparency aware textures, etc. To this end, tools like QGIS [32] and VAPOR [24] offer various rendering presets to accommodate different visual styles but fail to render styles outside the preset domains and also struggle to scale to massive scientific datasets.

Neural rendering is another category of rendering methods [4, 5] that learns to adaptively and efficiently render stylized visualizations from diverse data representations. Neural rendering methods find applications in a variety of tasks in computer graphics such as interactive scene editing [3], novel view synthesis, and animation synthesis [40]. Furthermore, a few works [12, 41] demonstrate the ability

of neural rendering in the high-fidelity reconstruction of frames by reducing aliasing and accelerating the rendering frame rates in interactive video game applications.

Inspired by the success of neural rendering methods for high-quality and real-time applications, in this work, we propose an efficient neural rendering framework, called Neural Accelerated Renderer (NAR), that learns to modify the forward-rendered PC visualizations to include the required visual constructs for high-quality scientific data visualization. We initially render with a compute shader-based multi-stream PC rasterizer, which we call Multi-Stream Rasterizer (MSR), and further refine with a neural network. Our rasterizer handles the workload of multiple data streams of high-resolution PC data from massive scientific simulations. Furthermore, we demonstrate that our method can visualize a variety of scientific PCs with various desired visualization styles, such as static vector fields, particle trajectories, and visual photometric scans. In this work, our primary contributions are as follows:

- **Efficient Scientific Data Rendering:** We introduce an efficient multi-stream PC rasterizer for accurately managing multiple data streams from vast scientific PC datasets.
- **High-Quality Neural Post-Processing:** NAR seamlessly blends various visual effects into the visualizations with end-to-end learnable neural rendering constructs.
- **Extensive Evaluation:** We illustrate the advantages of our framework over state-of-the-art methods to improve performance and rendering quality through extensive evaluation on various PCs.

2. Related Works

2.1. Scientific Point Cloud Visualization

Augmenting PC data with diverse information streams helps to visualize and understand various phenomena in different fields. Augmenting meteorological parameters (temperature, wind speed, humidity, etc.) for atmospheric vector fields visualization [11, 34], adding kinematic properties of subatomic particles in collider experiments in physics [29], and PC based characterization of binding sites in viruses [8] highlight the versatility of PCs. In practice, many visualization tools [9, 24, 32] provide the functionality to render and process PCs. However, tools such as [9, 24] fail to handle large amounts of high-resolution PC data. In this work, we choose the PC as a suitable representation for efficient scientific visualization at scale.

2.2. Interactive High-Quality Visualization at Scale

Owing to their reduced vertex buffer usage and low bandwidth requirements, point primitives have been a primary choice in real-time visualization of large scenes both in research [20, 28, 37] and practice (Potree [39], CloudCom-

pare [1], QGIS [32]). RayCaching [28] is a point-based isosurface rendering method that caches points computed by ray intersections with scene elements and then renders through splatting. Compute Rasterizer (CR) [37] is another high-performance PC renderer for massive datasets that uses compute shaders to avoid the use of conventional point primitive APIs (such as `GL_POINTS` in OpenGL and WebGL) and the accompanying inefficiencies of the standard graphics pipeline. This allows CR to improve the color quality, by reducing aliasing artifacts, and rendering speed, by proposing various optimizations on the buffers and vertex orders. Although these renderers are performant, they require explicit post-processing to render visual effects, which our method achieves via learning.

2.3. Neural Point Cloud Rendering

Point-based graphics has been a popular paradigm for visualization [22] using points [23] and surfels/splats [31, 44] as modeling primitives. More recently, extending on the idea of neural deferred rendering [40] to PCs, [3] proposed a neural point-based graphics (NPBG) approach for rendering visual scenes reconstructed with images. Since then, many works [25, 33, 36] have expanded this idea for efficient and high-quality visual scene rendering. [33] avoids optimizing per-point neural descriptors and, instead, predicts the neural descriptors directly from input views. [36] augments the NPBG rasterizer with a differentiable renderer to learn image parameters such as exposure, white balance, and camera response function. To extend NPBG’s capability to larger visual scenes, [25] develops an efficient strategy to sample and process a sparse PC to generate high-quality renderings. These methods compute the PCs or equivalent neural representations from the input images using structure-from-motion or learning-based methods. Our work uses actual PCs, typically from scientific simulations or observations, as input, avoiding numerical inaccuracies in the PC data. Other neural PC rendering works [10, 15] focus on high-quality PC rendering using expensive methods such as 3D CNNs and multiscale radiance fields, which makes these methods unsuitable for real-time rendering of large PCs. Most of these previous works render PCs of visual scenes. However, unlike visual data, scientific datasets lack rich textures and semantic structures offering learning challenges. This work enables direct real-time visualization of the massive scientific PC in its entirety.

3. Neural Accelerated Renderer

3.1. Framework Overview

In this work, we accelerate a given conventional renderer to visualize large-scale PCs in real-time. Figure 2 shows an overview of the training and the inference phases of NAR. We provide flexibility to choose the high-quality renderer,

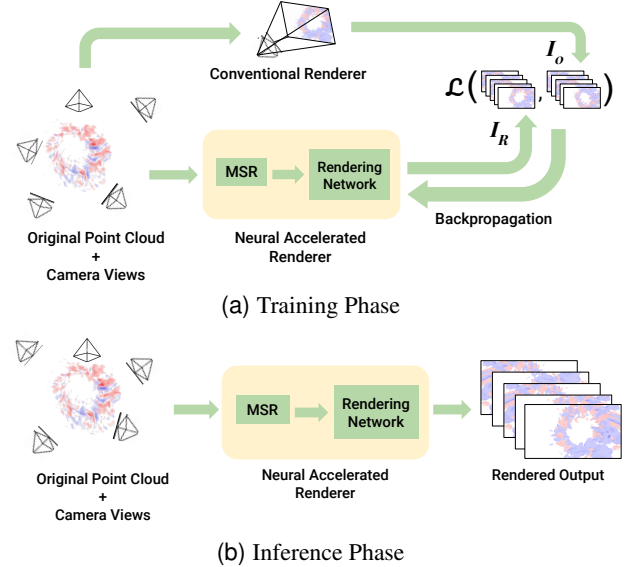


Figure 2. NAR Overview. (a) We train NAR with the large high-resolution scientific PC data and a preferred renderer (Gaussian Splatting forward renderer [20] in our case) for learning geometry and appearance respectively. I_O and I_R represent the rendering from the conventional renderer and NAR respectively. (b) We only use the original (or modified) PC to render real-time high-quality renderings based on the user’s viewing directions for inference.

as per the user’s requirements, to create training datasets that NAR learns to emulate. Thus, after the offline training phase, we can deploy NAR to render high-quality visualizations of the original or even a modified PC (such as a subsampled one) in real-time. Figure 3 presents a detailed structure of NAR, which has two major components - a high-performance multi-stream rasterizer (MSR) and a rendering network. In this section, we present the details of each of the components. We also provide additional details on the training data generation in section 4.2.

3.2. Multi-Stream Rasterizer

Unlike conventional renderers that render color and depth per pixel, we consider the various data streams to visualize scientific PCs. For example, storm simulation data (refer to Figure 1(b)) in a Lagrangian representation contains fields such as atmospheric pressure, temperature, and pressure-altitude. We use MSR to render points that are rich in geometric information and simulated or measured physical parameters. This serves as feature-rich input for the rendering network in the next stage of NAR.

We extend the capabilities of high-performance CR compute shaders [37] with multi-stream rasterization to process the multi-dimensional scientific data. We perform rendering in two stages - render and resolve. The render stage

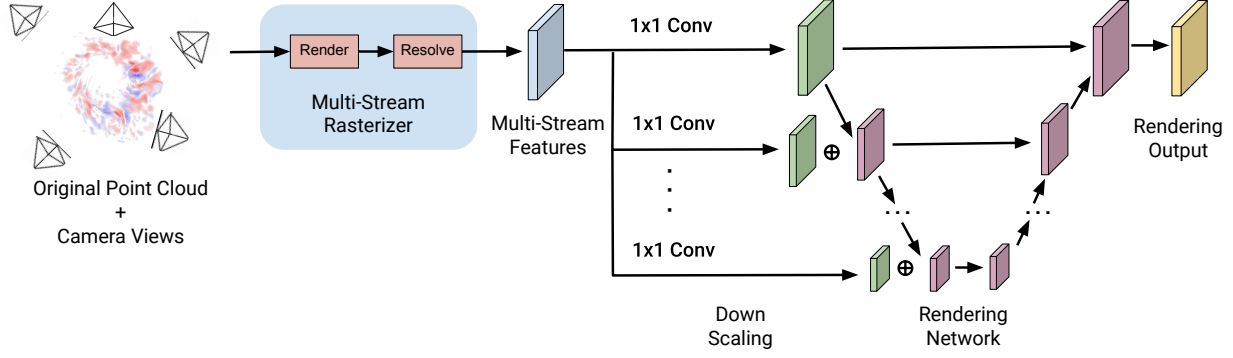


Figure 3. Details of the NAR. We take the input view and the PC to render view-dependent PC features with an MSR and pass these features to our rendering network, a U-Net [35], to generate final renderings. Before passing to the U-Net, we down scale and apply a 1×1 -Convolution (retaining the number of channels) to the multi-stream features and concatenate (\oplus) them to the first U-Net blocks at the respective resolutions. (Green blocks: down scaled and 1×1 convolved multi-stream features, Pink blocks: U-Net block outputs.)

transforms the points to screen space and the resolve stage processes points as OpenGL textures. While projecting $\sim 100M$ visible points onto a few million pixels, occlusions will occur due to the pigeonhole principle. Therefore, we render the closest visible points with the lowest depth via early z-buffer testing to reduce rendering costs. However, unlike CR, we save on the computation cost by avoiding color averaging of the overlapping points. We can process different information streams based on the visualization needs with MSR. We use the velocity vector properties for visualizing static vector field and particle trajectory (see section 4.5.3). For rendering terrain data, we also compute the projected point (splat) radius with MSR (see section 4.2). Furthermore, we support different quantities of streams (currently up to 8) and formats (uint8 and fp32) for multi-stream data as per the visualization needs.

3.3. Rendering Network and Training Details

We use a U-Net [35] with gated convolution [43] as the rendering network. The network takes the MSR rendered feature image and post-processes the image to generate multi-resolution feature images (see Figure 3). Apart from rendering various visual effects, the benefit of a separate neural renderer (or a post-processing operator) is its invariance to the coordinate space conventions and transformations on the input 3D PC. Methods such as [3] effectively learn the local scene geometry and appearance with point-wise neural descriptors. However, this severely limits scalability to a large number of points. Instead, we use a 1×1 convolution layer to efficiently model the view-dependent local appearance around a point in the PC after projection to the image plane, removing the dependency on PC size. Unlike [3], we end up learning the point descriptors of the visible points only. Thus, 1×1 convolution offers a mechanism to filter the neural

descriptors based on the viewpoints. However, this does not imply NAR’s inability to learn the descriptors for the occluded points. If transparency is required in the final rendering, our method implicitly learns a combined descriptor of all the occluded points rendered to a common pixel using the ground truth images from the reference transparency-aware renderer.

We downsample the output of 1×1 convolution to create a set of multiscale images at different resolutions (specifically at 5 resolutions each downsampled by a factor of 0.5). This serves as a proxy to learn the implicit level of details (LoD) from the input PC. We then concatenate these multiscale images to the corresponding resolutions of interleaved first blocks of the U-Net encoder. Finally, we train the rendering network with the following objective function:

$$\mathcal{L}(I_R, I_O) = \mathcal{L}_{perc}(I_R, I_O) + \alpha \mathcal{L}_{reco}(I_R, I_O) + \beta \mathcal{L}_{\nabla}(I_R, I_O), \quad (1)$$

where I_R and I_O are the NAR output and the reference images from the conventional renderer, respectively. We use perception loss [18], \mathcal{L}_{perc} , for visual structure learning and the reconstruction loss (pixel-wise L_2 norm), \mathcal{L}_{reco} , for color consistency. For generating smooth rendering, we use the 2D total variation loss, \mathcal{L}_{∇} . α and β are the optimization constants. More hyperparameter details in Section 7 (supplementary).

4. Experiments and Results

4.1. Datasets and Evaluation Metrics

We use two PCs - *Hurricane* (408K points), based on the large eddy simulation of hurricanes [13, 14], and *Storms* (45M points), produced from an atmospheric trajectory model using NASA GEOS winds [2]. Datasets contain

latitude and longitude coordinates of the points, their 3D velocity profiles, pressure, temperature and potential temperature, and pressure altitude fields from hurricane and storm simulations worldwide. We also test our framework on a significantly larger Morro Bay PC [38] (350M points), a LIDAR scan of a large terrain area. These datasets represent different types of scientific 3D data with varied visualization requirements. Specifically, Hurricane represents a temporal snapshot of a velocity vector field, Storms is a simulation of particle trajectories under different atmospheric vector field influences, and Morro Bay is a photometric snapshot of a large 3D surface.

We evaluate the rendering quality using peak signal-to-noise ratio (PSNR) and structural similarity index (SSIM) metrics and also report the per-frame latency and frame rates to measure the computational efficiency. We also report the memory footprint to measure the memory requirements of the methods. All the experiments use an NVidia GeForce RTX 2080 Ti GPU and RTX A6000 GPU (when the GPU and shared memory requirements exceed 13 GB).

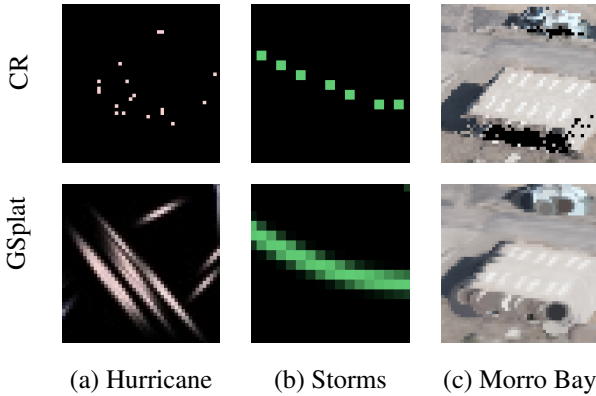


Figure 4. Gaussian splatting rendering effects for PC visualization and training data creation.

4.2. Training Data Generation

For training NAR, we use renderings from Gaussian splatting renderer [20]. This renderer provides control over the geometry, color, and transparency of the point samples by treating each point as a Gaussian splat resulting in various rendering effects used to generate training examples (see Figure 4). For each point, \mathbf{x} , in the Hurricane and Storms, we include the point orientation to visualize the vector field, $\mathbf{F} : \mathbb{R}^3 \rightarrow \mathbb{R}^3$, by elongating Gaussians, $\mathcal{N}(\mathbf{x}, \Sigma)$, along the direction of the vector, $\mathbf{v} = \mathbf{F}(\mathbf{x})$. The covariance matrix, Σ , is computed as $\Sigma = \mathbf{R}\mathbf{S}\mathbf{R}^T$, with $\mathbf{S} = \text{diag}(s, 1, 1)$, (and generally the stretch factor $s \gg 1$) as the scaling matrix and \mathbf{R} as the orthonormal rotation matrix whose dominant eigenvector is \mathbf{v} . For the Morro Bay dataset, we also

control the splat sizes by scaling the Gaussian covariance matrices isotropically, which is useful for filling holes in the image. For hole filling, we set the splat radius as the average distance between a point and its four nearest neighbors. Furthermore, we carefully select viewpoints to cover all the scene elements (Section 6 in the supplementary).

4.3. Comparative Evaluation

Rendering Performance: We compare our method’s performance, specifically latency, memory footprint, and rendering quality, against the following state-of-the-art renderers, (in Table 1 and Figure 5):

- **Gaussian Splatting (GSplat)** [20, 44]: This forward renderer rasterizes Gaussians for each point in the PC allowing easy manipulation of the point geometry with high-quality rendering.
- **Compute Rasterizer (CR)** [37]: We compare the early-z buffer tests CR variant without vertex order modification for Hurricane and Storms data and use Morton-ordered Morro Bay data. CR is optimized for both low-latency and high-quality colors mitigating anti-aliasing artifacts.
- **NPBG** [3]: This neural PC rendering method uses a simple OpenGL renderer with learnable point descriptors.

NAR balances rendering latency and quality and outperforms the other renderers in rendering quality across all the datasets. It is only slower than high-performance CR which has lower visual fidelity than NAR, especially in sparser regions, as it renders points as pixels. GSplat has the highest image quality as it is our reference renderer. However, GSplat also has a high rendering latency due to the increased α -blending overheads (involving sorting) in large PCs. NPBG, an NN based method, has a better rendering quality than CR but is memory intensive as it uses per-point descriptors. NPBG also has a higher latency as its OpenGL rasterizer uses `GL_POINTS` primitive to render frames at multiple image resolutions making it unsuitable for real-time rendering of large full-resolution PCs.

4.4. Generalizability of NAR

We explore the generalizability aspects of NAR to show its broader applicability. To this end, we train NAR on a source PC to visualize another target PC with similar visualization requirements. For this experiment, we split the Storms dataset by time slices of the trajectories. Of the 301 time slices, we use the first 200 time slices of trajectory for the source PC and the rest 101 slices form the target PC. We also increase the viewpoint grid resolution (see Section 6 in the supplementary materials) to 15×15 , obtaining more training views. We achieve an average PSNR of 30.23 and an average SSIM of 0.903 (w.r.t. GSplat) for the target PC. Figure 6 shows the NAR rendering of the source and target PCs from the same views. Unlike NPBG [3], which cannot

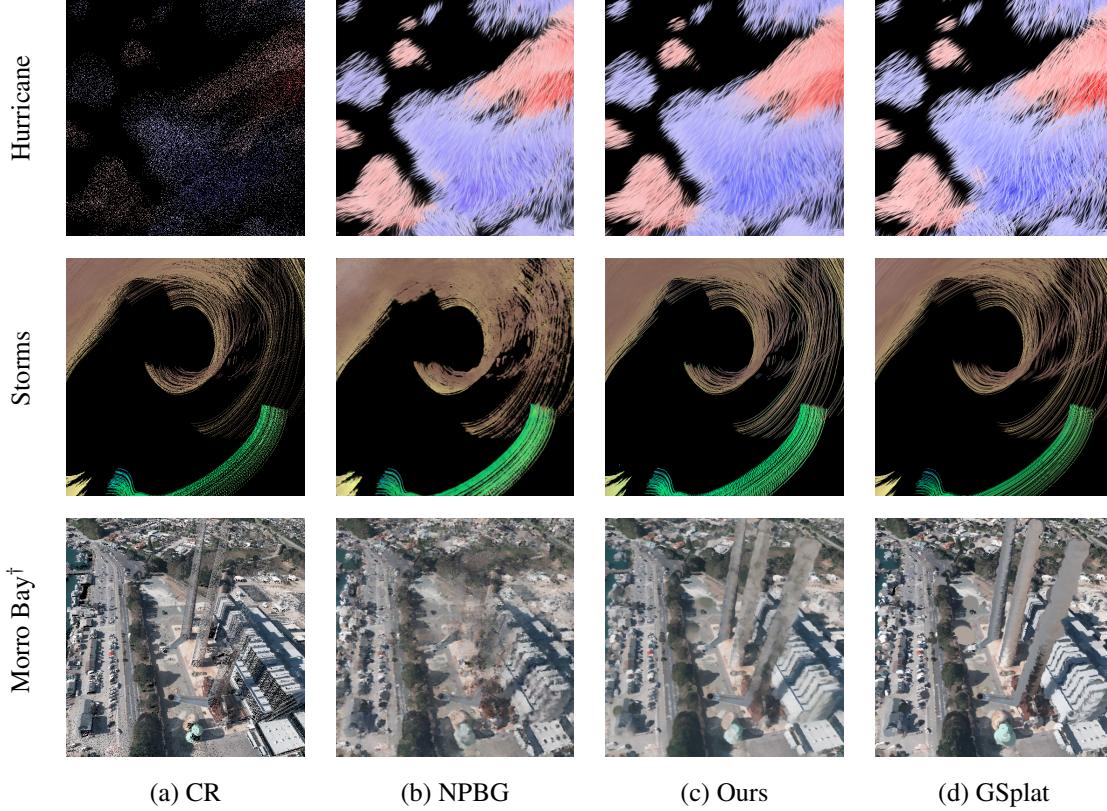


Figure 5. Qualitative comparison of different renderers. NPBG and NAR are trained on GSplat renderings. [†]GSplat and NPBG used 0.5× and 0.1× the original number of MorroBay points, respectively, due to memory constraints. More results in Section 9 of the supplementary.

render a variable number of points during inference, NAR effectively learns the required post-processing effects irrespective of the specific properties of the source / target PC.

4.5. Ablation Studies and Discussions

4.5.1 Ablation of the Framework Components

Table 2 shows the breakdown of the runtimes of different components of our framework. *Transfer + Proc.* denotes the time required to convert OpenGL buffers to CUDA tensors, stream-wise processing, and downsampling the MSR output into 5 different resolutions. We observe that the U-Net inference is a major factor that causes latency. We implement the neural renderer in PyTorch [30] without any neural acceleration. However, we observe a limited speedup and memory savings under certain cases on quantizing the U-Net (Section 8 in supplementary materials).

Using 1×1 -Conv over using no descriptors and using per-point learnable neural descriptors (similar to [3]) is beneficial (see Table 3). Naively downsampling the feature images with neural descriptors results in large errors in the gradients. Thus, per-point descriptors require rendering the multi-scale feature images at 5 different resolutions result-

ing in a significant delay. Thus, using per-point descriptors slightly improves the rendering quality at the cost of $\sim 4\times$ rendering delay. In Table 3, columns *PC* and *Network* show the memory requirements for PC loading and NN parameters, respectively. *PC* is calculated as $N \sum_i B_i$, where N is the number of points, B_i is the number of bytes for representing the i^{th} data stream. Both 1×1 -Conv and *No Descriptors* variants use point coordinates (3D float vector), byte-packed RGB, depth (single float) and velocity (4D float vector, see *Vel2D* in section 4.5.3). *Per-point Descriptor* variant represents each point with point coordinates (3D float vector), point indices (integers), and 4D learnable per-point descriptors (floats). *Per-point Descriptors* variant, although with a marginally better rendering quality than 1×1 -Conv, is unscalable as the memory requirements of the network depend on the number of points. 1×1 -Conv improves the rendering quality and speed almost matching the memory overhead of the *No Descriptors* case.

4.5.2 Effects of Point Cloud Resolution on Rendering Performance

PC resolution is crucial for PC rendering. For example, a high-resolution PC can be rendered with high quality as it

| Method | PSNR | SSIM | Latency (in ms) / fps | Memory (in GB) |
|--------------------------------|--------------|--------------|--------------------------|-------------------|
| <i>Hurricane (408K points)</i> | | | | |
| CR | 9.57 | 0.623 | 1.01 / 989.84 | 0.80 |
| GSplat | - | - | 28.86 / 34.65 | 0.40 |
| NPBG | 22.76 | 0.788 | 13.64 / 73.32 | 1.00 |
| Ours | 24.65 | 0.813 | 6.97 / 143.44 | 1.70 |
| <i>Storms (45M points)</i> | | | | |
| CR | 17.92 | 0.707 | 1.03 / 966.83 | 1.13 |
| GSplat | - | - | 3515 / 0.28 | 7.10 |
| NPBG | 24.29 | 0.854 | 80.07 / 12.49 | 4.90 |
| Ours | 25.23 | 0.849 | 6.58 / 152.01 | 3.10 |
| <i>Reduced Morro Bay</i> | | | | |
| GSplat* | - | - | 5536 / 0.18 | 23.93 |
| NPBG† | 23.76 | 0.683 | 64.82 / 15.428 | 5.98 |
| <i>Morro Bay (350M points)</i> | | | | |
| CR | 17.28 | 0.312 | 1.05 / 951.09 | 5.79 |
| Ours | 24.49 | 0.683 | 7.91 / 126.38 | 12.73 |

Table 1. Comparison of rendering quality (w.r.t GSplat rendering), latency, and memory footprints of different renderers. Note: we use the original PC resolution for rendering. (*used $0.5\times$ and † used $0.1\times$ the number of points due to memory restrictions)

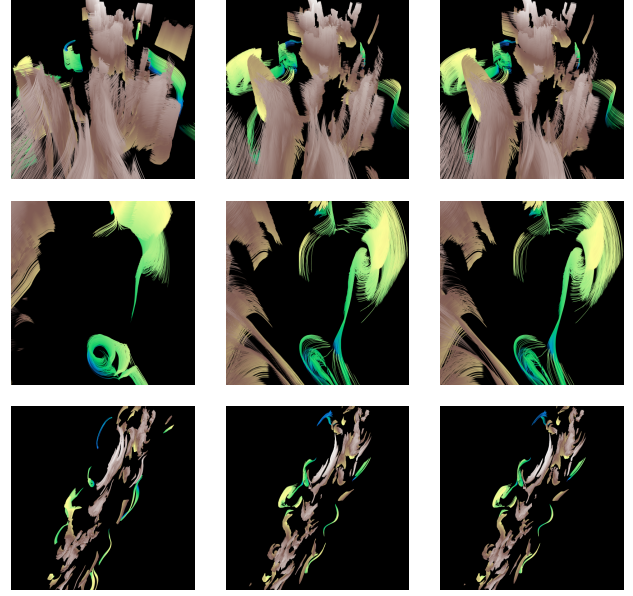
| Component | Hurricane | Storms | Morro Bay |
|------------------|-----------|--------|-----------|
| MSR | 0.104 | 0.106 | 0.122 |
| Transfer + Proc. | 1.781 | 1.735 | 2.026 |
| U-Net | 4.504 | 4.692 | 5.456 |

Table 2. Runtimes (in ms) of the different NAR components evaluated at full PC resolution with 2000×1328 frame resolution.

| | No Descriptors | Per-point Descriptors | 1×1 Conv |
|-------------------|-------------------|--------------------------|----------------------|
| PSNR | 22.24 | 22.56 | 22.42 |
| SSIM | 0.761 | 0.812 | 0.814 |
| Runtime (ms) | 7.077 | 24.88 | 6.971 |
| PC Memory (MB) | 14.71 | 13.08 | 14.71 |
| U-Net Memory (MB) | 7.73 | 14.35 | 7.74 |

Table 3. Ablation study of the U-Net variants evaluated on a full resolution Hurricane dataset with 2000×1328 frame resolution.

typically has denser regions with rich textures. However, rendering such high-resolution PCs is expensive and slow. NAR allows using a down-sampled PC while maintaining the rendering quality and reducing memory footprints and rendering latency. We show this by varying the input PC



(a) Source PC (b) Target PC (c) GSplat

Figure 6. Generalizability of NAR. NAR learns the post-processing effects from the source PC, (a), for visualizing the target PC, (b), irrespective of diverse PC geometry and properties. (c) GSplat renderings from the corresponding views for reference.

resolution and recording the rendering performances. We reduce the PC resolution by uniformly sub-sampling the PC by different fixed factors. However, we still use I_O generated with the full resolution PC while training.

With decreasing PC resolution (or increased sparsity), rendering quality dips but frame rates are nearly constant (see Table 4 and Figure 7). The dip in rendering quality is caused by the increased low-density regions in the PC which are harder to interpolate for the neural renderer. This could be observed in the drastic fall of the rendering qualitative metrics for a sparse Hurricane dataset. Neural renderer’s dependence on the number of points in the projected frame, and not on the overall points in the PC, explains the near-constant frame rates, irrespective of the dataset used. Thus, even with lower-resolution PCs, NAR renders dense high-quality visualizations at increased frame rates.

4.5.3 Influence of Data Streams on Rendering Quality

In Table 5 (and Figure 11 of supplementary), we pass different combinations of streams and study their effects on neural rendering quality to specifically visualize the velocity vector, \mathbf{v} , associated with each point. Here, RGB are the color channels depicting the photometric properties of the data, D is the scene depth w.r.t the camera, $Vel3D$ represents a 4D vector $\mathbf{v}_{3D} = (v_x, v_y, v_z, |\mathbf{v}|)$ where v_x, v_y, v_z

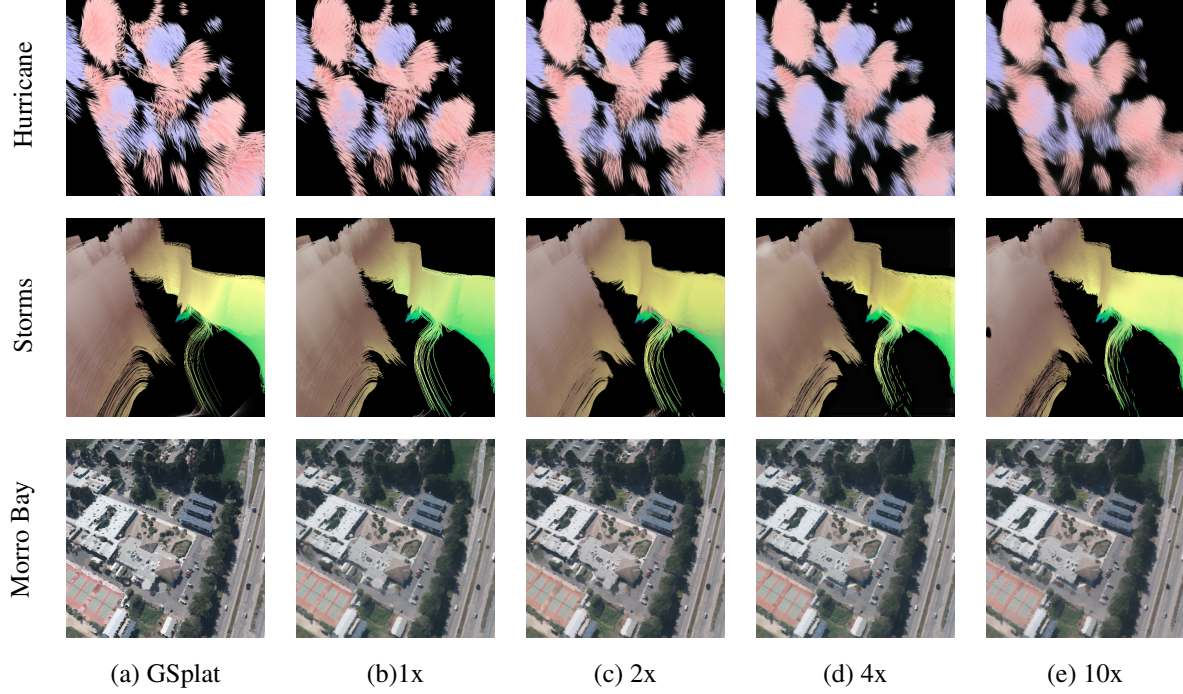


Figure 7. Qualitative results of NAR at various PC sparsity when compared with the GSplat ground truth. More results in Section 9 of the supplementary materials.

| Dataset | Sparsity | PSNR | SSIM | Latency (in ms) / fps |
|--------------------------------|----------|--------------|--------------|--------------------------|
| <i>Hurricane</i> (408K pts) | 1x | 24.65 | 0.813 | 6.97 / 143.44 |
| | 2x | 22.61 | 0.743 | 6.77 / 147.75 |
| | 4x | 21.19 | 0.701 | 6.79 / 147.22 |
| | 10x | 20.21 | 0.673 | 6.89 / 145.17 |
| <i>Storms</i> (45M pts) | 1x | 25.23 | 0.849 | 6.58 / 152.01 |
| | 2x | 24.29 | 0.840 | 6.62 / 150.99 |
| | 4x | 23.62 | 0.792 | 7.07 / 141.44 |
| | 10x | 23.40 | 0.706 | 6.79 / 147.22 |
| <i>Morro Bay</i> (350M pts) | 1x | 24.49 | 0.683 | 7.91 / 126.38 |
| | 2x | 24.09 | 0.686 | 7.36 / 135.92 |
| | 4x | 23.73 | 0.641 | 7.18 / 139.31 |
| | 10x | 23.18 | 0.608 | 7.15 / 139.92 |

Table 4. Evaluating the effect of PC sub-sampling on performances of the proposed method on different datasets.

are the 3D velocity components, and $Vel2D$ is another 4D vector $\mathbf{v}_{2D} = (v'_x, v'_y, \theta, |\mathbf{v}'|)$, where \mathbf{v}' is the perspective projected \mathbf{v} vector and v'_x, v'_y are the 2D components of \mathbf{v}' , and θ is the angle of inclination of \mathbf{v}' in the image plane. We observe a marginal improvement in rendering quality by adding depth information. Passing $Vel2D$ to the U-Net performs the best as $Vel2D$ explicitly encodes the geomet-

ric cues of the point. $Vel3D$ does not improve the rendering quality as it is view-independent information and, thus, is less informative than the perspective projected $Vel2D$.

| Streams | PSNR | SSIM |
|-------------|--------------|--------------|
| RGB | 23.03 | 0.732 |
| RGB+D | 23.19 | 0.741 |
| RGB+Vel2D | 25.13 | 0.812 |
| RGB+D+Vel3D | 22.92 | 0.754 |
| RGB+D+Vel2D | 24.65 | 0.813 |

Table 5. Evaluating our framework with different input data streams of the Hurricane dataset at full PC resolution.

5. Conclusions

We present NAR, an efficient solution for challenging real-time high-fidelity visualization of massive scientific PCs. NAR is ideal for diverse scientific visualizations such as complex Lagrangian dynamics and a massive photometric terrain scan. We demonstrate the ability to render 350M points (12.7GB) at >126 fps (i.e., a throughput of over 44B points/second) on an RTX 2080 Ti GPU. NAR is generalizable for different PCs and retains substantial rendering quality even when used with a subsampled PC, ultimately reducing memory requirements. We evaluate and discuss the different optimization choices through an ablation study

to significantly reduce rendering latency and memory footprints. Given the low motion-to-photon latency and high fidelity, we expect NAR to be foundational for immersive visualizations to analyze scientific phenomena.

References

- [1] *CloudCompare - 3D point cloud and mesh processing software*. <https://www.danielgm.net/cc/>. Accessed May'24.
- [2] *Goddard Earth Observing System (GEOS)*. https://gmao.gsfc.nasa.gov/GEOS_systems/.
- [3] Kara-Ali Aliev, Artem Sevastopolsky, Maria Kolos, Dmitry Ulyanov, and Victor Lempitsky. Neural point-based graphics. In *Computer Vision—ECCV 2020: 16th European Conference, Glasgow, UK, August 23–28, 2020, Proceedings, Part XXII 16*, pages 696–712. Springer, 2020.
- [4] Joshua Aurand, Raphael Ortiz, Silvia Nauer, and Vinicius C Azevedo. Efficient neural style transfer for volumetric simulations. *ACM Transactions on Graphics (TOG)*, 41(6):1–10, 2022.
- [5] Matthew Berger, Jixian Li, and Joshua A Levine. A generative model for volume rendering. *IEEE transactions on visualization and computer graphics*, 25(4):1636–1650, 2018.
- [6] Andrea Brambilla, Robert Carnecky, Robert Peikert, Ivan Viola, and Helwig Hauser. Illustrative flow visualization: State of the art, trends and challenges. *Visibility-oriented Visualization Design for Flow Illustration*, 2012.
- [7] Roxana Bujack and Ariane Middel. State of the art in flow visualization in the environmental sciences. *Environmental Earth Sciences*, 79(2):65, 2020.
- [8] Research Communities by Springer Nature. Innophore’s 3D point clouds provide a head start in monitoring emerging SARS-CoV-2 variants — communities.springernature.com. <https://communities.springernature.com/posts/test-9570e791-9a39-4e77-9e41-3364d7c3e3d5>. [Accessed 05-2024].
- [9] Blender Online Community. *Blender - a 3D modelling and rendering package*. Blender Foundation, Stichting Blender Foundation, Amsterdam, 2018.
- [10] Peng Dai, Yinda Zhang, Zhuwen Li, Shuaicheng Liu, and Bing Zeng. Neural point cloud rendering via multi-plane projection. In *Proceedings of the IEEE/CVF Conference on Computer Vision and Pattern Recognition*, pages 7830–7839, 2020.
- [11] Suzana Djurcilov and Alex Pang. Visualizing sparse gridded data sets. *IEEE Computer Graphics and Applications*, 20(5): 52–57, 2000.
- [12] Andrew Edelsten, Paula Jukarainen, and Anjul Patney. Truly next-gen: Adding deep learning to games and graphics. *NVIDIA Sponsored Sessions (Game Developers Conference)*, 2019.
- [13] Stephen R Guimond and Sydney Sroka. Large eddy simulations of hurricane intensification. In *33rd Conference on Hurricanes and Tropical Meteorology*. AMS, 2018.
- [14] Stephen R Guimond, Jon M Reisner, Simone Marras, and Francis X Giraldo. The impacts of dry dynamic cores on asymmetric hurricane intensification. *Journal of the Atmospheric Sciences*, 73(12):4661–4684, 2016.
- [15] Tao Hu, Xiaogang Xu, Shu Liu, and Jiaya Jia. Point2pix: Photo-realistic point cloud rendering via neural radiance fields. In *Proceedings of the IEEE/CVF Conference on Computer Vision and Pattern Recognition*, pages 8349–8358, 2023.
- [16] Victoria Interrante. Harnessing natural textures for multi-variate visualization. *IEEE Computer Graphics and Applications*, 20(06):6–11, 2000.
- [17] David M. Johnson. Introduction to and review of simulator sickness research. Technical report, U.S. Army Research Institute, 2005.
- [18] Justin Johnson, Alexandre Alahi, and Li Fei-Fei. Perceptual losses for real-time style transfer and super-resolution. In *Computer Vision—ECCV 2016: 14th European Conference, Amsterdam, The Netherlands, October 11–14, 2016, Proceedings, Part II 14*, pages 694–711. Springer, 2016.
- [19] Daniel F Keefe, Daniel Acevedo, Jadrian Miles, Fritz Drury, Sharon M Swartz, and David H Laidlaw. Scientific sketching for collaborative vr visualization design. *IEEE Transactions on Visualization and Computer Graphics*, 14(4):835–847, 2008.
- [20] Bernhard Kerbl, Georgios Kopanas, Thomas Leimkühler, and George Drettakis. 3d gaussian splatting for real-time radiance field rendering. *ACM Transactions on Graphics*, 42(4), 2023.
- [21] Diederik P Kingma and Jimmy Ba. Adam: A method for stochastic optimization. *arXiv preprint arXiv:1412.6980*, 2014.
- [22] Leif Kobbelt and Mario Botsch. A survey of point-based techniques in computer graphics. *Computers & Graphics*, 28(6):801–814, 2004.
- [23] Marc Levoy and Turner Whitted. The use of points as a display primitive. 1985.
- [24] Shaomeng Li, Stanislaw Jaroszynski, Scott Pearse, Leigh Orf, and John Clyne. Vapor: A visualization package tailored to analyze simulation data in earth system science. *Atmosphere*, 10(9):488, 2019.
- [25] Zhuopeng Li, Lu Li, and Jianke Zhu. Read: Large-scale neural scene rendering for autonomous driving. In *Proceedings of the AAAI Conference on Artificial Intelligence*, pages 1522–1529, 2023.
- [26] Nina A Maksimova, Lehman H Garrison, Daniel J Eisenstein, Boryana Hadzhiyska, Sownak Bose, and Thomas P Satterthwaite. Abacussummit: a massive set of high-accuracy, high-resolution n-body simulations. *Monthly Notices of the Royal Astronomical Society*, 508(3):4017–4037, 2021.
- [27] Patrick Millais, Simon L Jones, and Ryan Kelly. Exploring data in virtual reality: Comparisons with 2d data visualizations. In *Extended abstracts of the 2018 CHI conference on human factors in computing systems*, pages 1–6, 2018.
- [28] Fredrik Nysjö, Filip Malmberg, and Ingela Nyström. Ray-caching: Amortized isosurface rendering for virtual reality. In *Computer Graphics Forum*, pages 220–230. Wiley Online Library, 2020.

- [29] Peter Onyisi, Delon Shen, and Jesse Thaler. Comparing point cloud strategies for collider event classification. *Physical Review D*, 108(1):012001, 2023.
- [30] Adam Paszke, Sam Gross, Soumith Chintala, Gregory Chanan, Edward Yang, Zachary DeVito, Zeming Lin, Alban Desmaison, Luca Antiga, and Adam Lerer. Automatic differentiation in pytorch. 2017.
- [31] Hanspeter Pfister, Matthias Zwicker, Jeroen Van Baar, and Markus Gross. Surfels: Surface elements as rendering primitives. In *Proceedings of the 27th annual conference on Computer graphics and interactive techniques*, pages 335–342, 2000.
- [32] QGIS Development Team. *QGIS Geographic Information System*. QGIS Association, 2024. <https://www.qgis.org>.
- [33] Ruslan Rakhimov, Andrei-Timotei Ardelean, Victor Lempitsky, and Evgeny Burnaev. Npbg++: Accelerating neural point-based graphics. In *Proceedings of the IEEE/CVF Conference on Computer Vision and Pattern Recognition*, pages 15969–15979, 2022.
- [34] Marc Rautenhaus, Michael Böttinger, Stephan Siemen, Robert Hoffman, Robert M Kirby, Mahsa Mirzargar, Niklas Röber, and Rüdiger Westermann. Visualization in meteorology—a survey of techniques and tools for data analysis tasks. *IEEE Transactions on Visualization and Computer Graphics*, 24(12):3268–3296, 2017.
- [35] Olaf Ronneberger, Philipp Fischer, and Thomas Brox. U-net: Convolutional networks for biomedical image segmentation. In *Medical image computing and computer-assisted intervention—MICCAI 2015: 18th international conference, Munich, Germany, October 5-9, 2015, proceedings, part III 18*, pages 234–241. Springer, 2015.
- [36] Darius Rückert, Linus Franke, and Marc Stamminger. Adop: Approximate differentiable one-pixel point rendering. *ACM Transactions on Graphics (ToG)*, 41(4):1–14, 2022.
- [37] Markus Schütz, Bernhard Kerbl, and Michael Wimmer. Rendering point clouds with compute shaders and vertex order optimization. *Computer Graphics Forum*, 40(4):115–126, 2021.
- [38] Markus Schütz, Bernhard Kerbl, and Michael Wimmer. Software rasterization of 2 billion points in real time. *Proceedings of the ACM on Computer Graphics and Interactive Techniques*, 5(3):1–17, 2022.
- [39] Markus Schütz, Stefan Ohrhallinger, and Michael Wimmer. Fast out-of-core octree generation for massive point clouds. *Computer Graphics Forum*, 39(7):13, 2020.
- [40] Justus Thies, Michael Zollhöfer, and Matthias Nießner. Deferred neural rendering: Image synthesis using neural textures. *Acm Transactions on Graphics (TOG)*, 38(4):1–12, 2019.
- [41] Lei Xiao, Salah Nouri, Matt Chapman, Alexander Fix, Douglas Lanman, and Anton Kaplanyan. Neural supersampling for real-time rendering. *ACM Transactions on Graphics (TOG)*, 39(4):142–1, 2020.
- [42] Wenhui Xiao, Rodrigo Santa Cruz, David Ahmedt-Aristizabal, Olivier Salvado, Clinton Fookes, and Leo Lebrat. Nerf director: Revisiting view selection in neural volume rendering. In *Proceedings of the IEEE/CVF Conference on Computer Vision and Pattern Recognition*, pages 20742–20751, 2024.
- [43] Jiahui Yu, Zhe Lin, Jimei Yang, Xiaohui Shen, Xin Lu, and Thomas S Huang. Free-form image inpainting with gated convolution. In *Proceedings of the IEEE/CVF international conference on computer vision*, pages 4471–4480, 2019.
- [44] Matthias Zwicker, Hanspeter Pfister, Jeroen Van Baar, and Markus Gross. Surface splatting. In *Proceedings of the 28th annual conference on Computer graphics and interactive techniques*, pages 371–378, 2001.

NARVis: Neural Accelerated Rendering for Real-Time Scientific Point Cloud Visualization

Supplementary Material

6. Selecting Viewpoints in Training Data

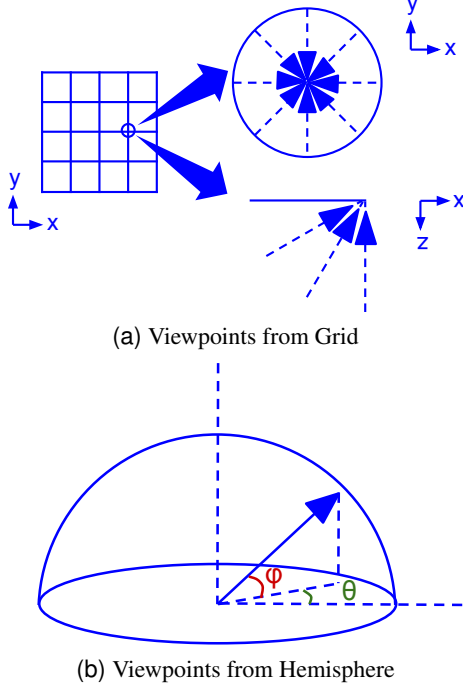


Figure 8. Strategies for Selecting Viewpoints for Training. Triangles in the diagram represent cameras with look-at vectors along the line passing through the base of the triangle.

Figure 8 shows the viewpoint sampling strategies for collecting the training and evaluation data at a 512×512 resolution. For all datasets, we select the viewpoints with two strategies. In the first strategy, we place our virtual cameras at the intersections of the 10×10 grid (15×15 for Hurricane) which is parallel to the x, y -plane of the PC bounding box at a constant predetermined height above the maximum z coordinate of the bounding box. At each grid location, we capture the views by rotating the camera about the z -axis at the interval of 45° (yaw) and also at the pitch levels 1° , 30° , and 60° . Optionally, we sample multiple such grids at different heights above x, y -plane for including multi-scale details of the PC. In the second strategy, we consider a hemisphere around the PC. The hemisphere is centered at the center of the PC bounding box and the radius of the hemisphere, r , is $0.75 \times$ of the PC bounding box diagonal. We then place the cameras on the hemisphere so that the polar coordinates of the cameras could be represented as (r, θ, ϕ) . Here, $\theta \in [0, 2\pi]$ sampled in the interval of $\pi/8$ ($\pi/16$ for

Hurricane) and $\phi \in [0, \pi/2]$ sampled in the interval of $\pi/16$ ($\pi/32$ for Hurricane). Also, note that our selection strategy is not rigorous in coverage. For a formal study on view selection strategies, refer to [42].

7. Training Hyperparameters

To facilitate the implementation of our rendering network, we comprehensively report some of the hyperparameters used in training. The multiresolution feature creation process utilizes a downscaling factor of 0.5 repeated for 5 scales, as described in the main text. In the objective function (Eq. 1), we set the coefficients α and β to 10^{-3} and 10^4 , respectively. We employ the Adam [21] optimizer with an initial learning rate of 10^{-3} . We train the network with a batch size of 16 for 100, 100, and 200 epochs for Hurricane, Storms, and Morro Bay respectively. We split the entire dataset into train and validation split of 9 : 1. We pass the input training images at a resolution of 512×512 . The training data used are rendered with a field of view of 60° and the near and far planes are placed at 0.1 and 2×10^5 units. We use a stretch factor, s , of 300 and 200 for Hurricane and Storms, respectively.

8. U-Net Quantization

We report the results (see Table 6) on applying a static quantization post-training on the U-Net weights and activations by reducing the precision from fp32 to fp16 . This reduces the memory requirements by a factor of $1.18 \times$ (on average across datasets) at the cost of a dip in rendering quality due to loss of precision. However, quantization marginally improves the inference speed only for larger PCs (see *Morro Bay*, Table 6) which saturate the GPU memory.

| Dataset | PSNR | SSIM | Latency (in ms) / fps | Memory (in GB) |
|-----------|-------|-------|--------------------------|-------------------|
| Hurricane | 24.62 | 0.833 | 7.97 / 125.48 | 1.40 |
| Storms | 19.73 | 0.808 | 7.88 / 126.90 | 2.80 |
| Morro Bay | 22.27 | 0.654 | 7.82 / 127.81 | 10.40 |

Table 6. Comparison of rendering quality (w.r.t GSplat rendering), latency, and memory footprints of NAR under quantization.

9. Additional Results

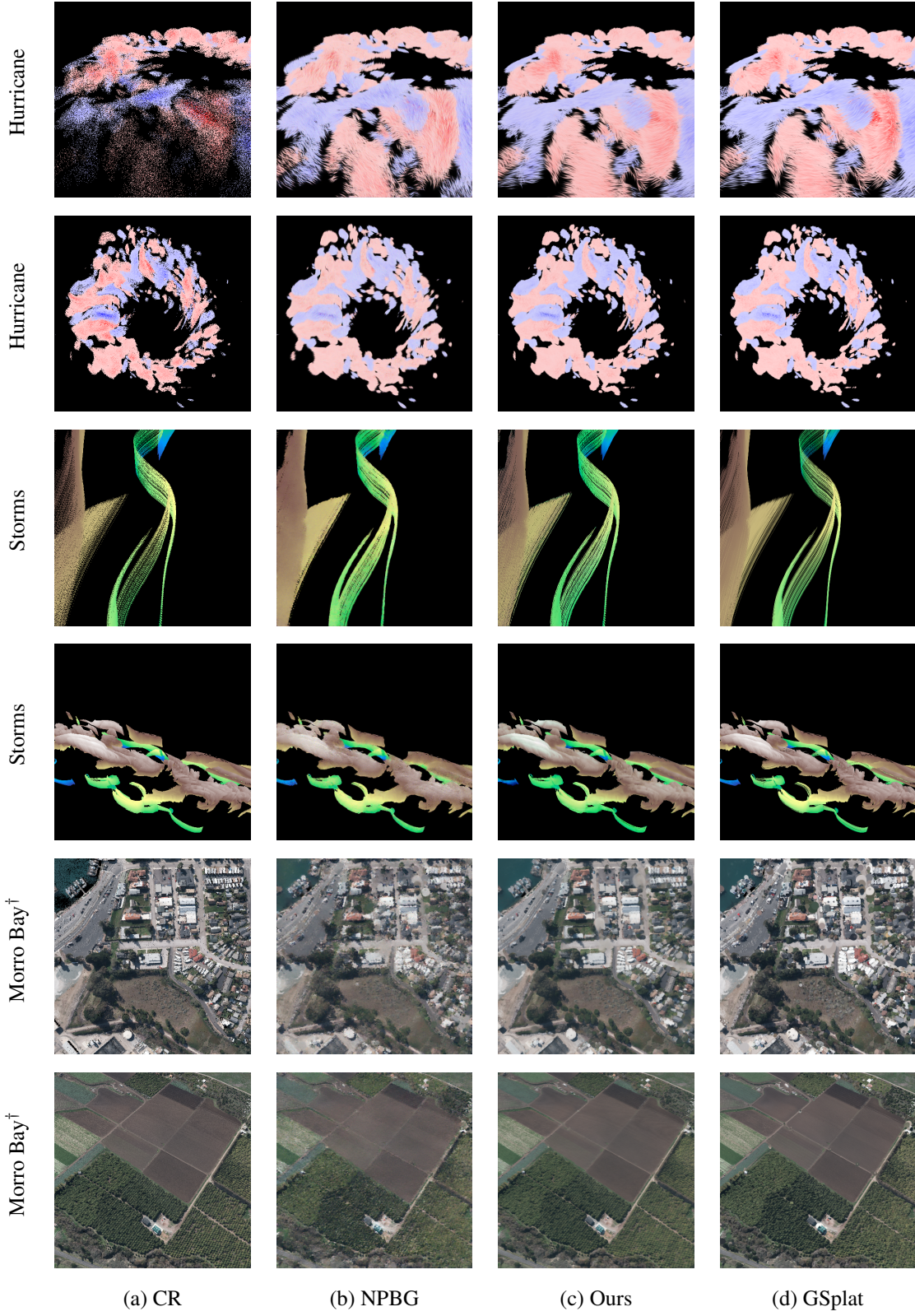
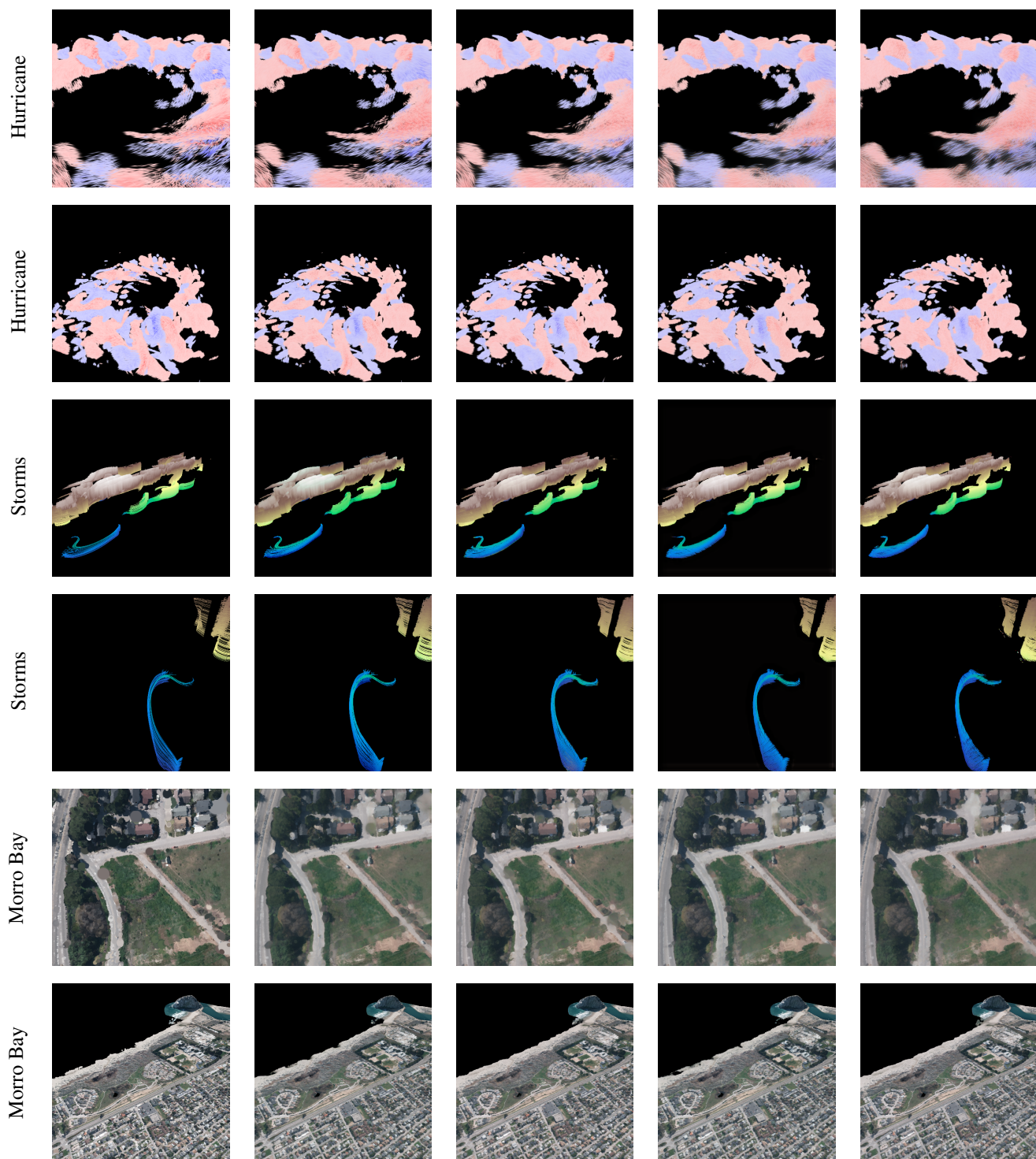


Figure 9. Qualitative comparison of different rendering methods. Both NPBG and NAR are trained on GSplat rendered images. [†]For the MorroBay dataset, GSplat and NPBG used 0.5 \times and 0.1 \times the original number of points, respectively, due to memory restrictions.



(a) GSplat

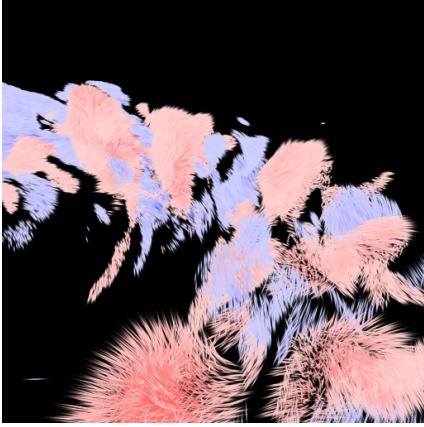
(b) 1x

(c) 2x

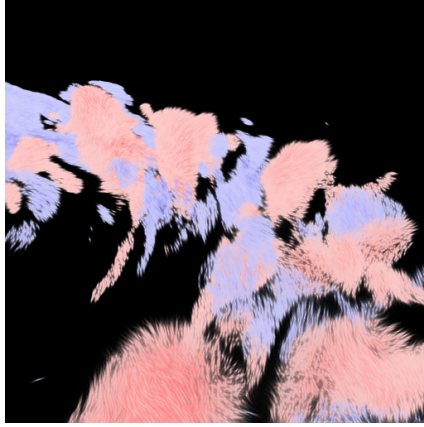
(d) 4x

(e) 10x

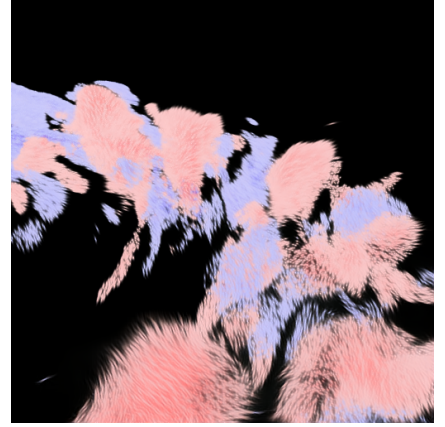
Figure 10. Qualitative results of NAR at various PC sparsity when compared with the GSplat ground truth.



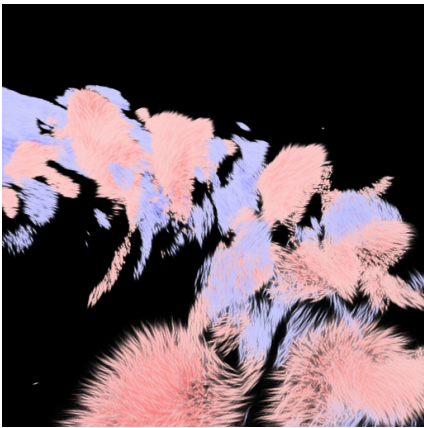
(a) GSplat



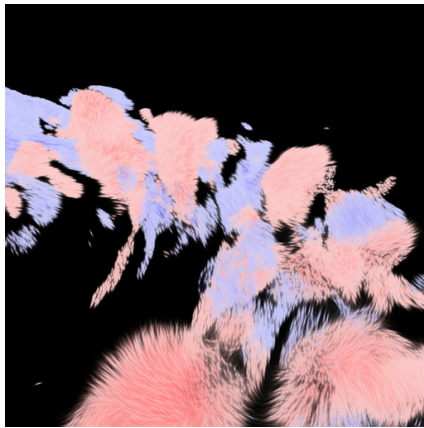
(b) RGB



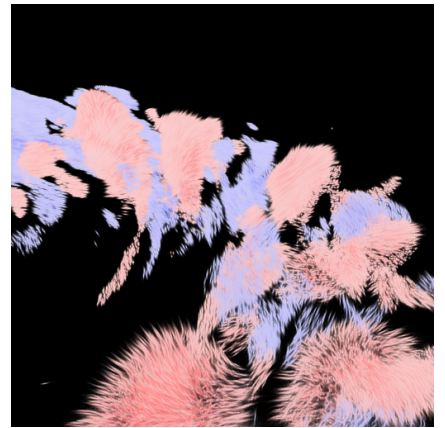
(c) RGB+D



(d) RGB+Vel2D



(e) RGB+D+Vel3D



(f) RGB+D+Vel2D

Figure 11. Qualitative results of NAR when UNet is trained with different input streams from MSR as discussed in Section 4.5.3.